International Journal of Modern Physics B
Vol. 37, No. 29 (2023) 2350258 (25 pages)
© World Scientific Publishing Company
DOI: 10.1142/S0217979223502582

World Scientific
www.worldscientific.com

Convective heat transference of non-Newtonian functional phase variation nano-encapsulated liquids

Farooq H. Ali[*], Hameed K. Hamzah[*], Saba Y. Ahmed[*], Muneer A. Ismael[†,§],
Zoubida Haddad[‡], Mohammad Ghalambaz[¶], Azher M. Abed[‖],
Khaled Al-Farhany[**], Wasim Jamshed[††,¶¶] and Mohamed R. Eid[§§,‡‡]

[*]*Mechanical Engineering Department, College of Engineering,*
University of Babylon, Babylon City, Hilla, Iraq

[†]*Mechanical Engineering Department, Engineering College,*
University of Basrah, Basra, Iraq

[‡]*Institute of Electrical and Electronic Engineering,*
University M'Hamed Bougara of Boumerdes, Boumerdes, Algeria

[§]*College of Engineering, University of Warith Al-Anbiyaa, Karbala, Iraq*

[¶]*Laboratory on Convective Heat and Mass Transfer,*
Tomsk State University, Tomsk, 634045, Russia

[‖]*Air Conditioning and Refrigeration Techniques Engineering Department,*
Al-Mustaqbal University College, Babylon 51001, Iraq

[**]*Department of Mechanical Engineering,*
University of Al-Qadisiyah, Al-Qadisiyah 58001, Iraq

[††]*Department of Mathematics,*
Capital University of Science and Technology (CUST),
Islamabad 44000, Pakistan

[‡‡]*Department of Mathematics, Faculty of Science,*
New Valley University,
Al-Kharga, Al-Wadi Al-Gadid 72511, Egypt

[§§]*Department of Mathematics, Faculty of Science,*
Northern Border University, Arar 1321, Saudi Arabia
[¶¶]*wasiktk@hotmail.com*

Received 31 August 2022
Revised 16 October 2022
Accepted 18 November 2022
Published 23 February 2023

Convective flowing and heat transference of non-Newtonian liquid comprising nano-encapsulated phase-changing material (NEPCM) suspensions, filled in a square cavity, is numerically investigated. The molecules of NEPCM are cored with n-octadecane, shelled by polymethylmethacrylate, and suspended in non-Newtonian fluid. The enclosure is insulated horizontally and heated vertically. Finite element method (FEM) is implemented for the numerical solution under different variables such as nanoparticles volume fraction ($0 < \emptyset < 0.05$), Stefan number ($\mathrm{Ste} = 0.2, 0.313, 0.5$), the heat capacity ratio (λ) of about (0.4), the temperature of fusion of the

---

[¶¶] Corresponding author.

NEPCM ($0 < \theta_f < 1$) and the density ratio (ρ_P/ρ_f) ($0.7 < \rho_P/\rho_f \leq 0.9$). The results show that the Nusselt quantity is related to the fusion temperature. An improvement in heat transference is observed when the fusion temperature deviates from the wall temperature, which is in the range of $0.25 < \theta_f < 0.75$. For all power law index values (n), a linear increase of the Nusselt number with the solid volume fraction is detected. The shear-thinning nanofluid ($n = 0.6$) demonstrates higher Nusselt number values than those of $n = 1$ and 1.4.

Keywords: Nanoencapsulation; non-Newtonian phase change; fusion temperature.

PACS number: 44.35.+c

Nomenclature

C_p : Specific heat (kJ/kg $\cdot$ K)
C_r : Heat capacity ratio
D_{ij} : Deformation rate tensor
f : Phase change behavior
g : Gravity acceleration (m/s^2)
h_{sf} : Latent heat fusion (kJ/kg)
i : Number of grid case
k : Thermal conductance (W/m $\cdot$ K)
M : Consistency
M_{eff} : Effective viscosity
n : Power law index
N : Mesh size
N_c : Thermal conductivity number
Nu : Nusselt number
p : Pressure (Pa)
$\check{P}$: Dimensionless pressure
Pr : Prandtl number (ν_f/α_f)
Q_t : Total heat (J)
Ra : Rayleigh number ($g\beta_{\text{bf}}L^3(T_h - T_\infty)t/\nu_{\text{bf}}\alpha_{\text{bf}}$)
Ste : Stefan number
T : Temperature (K)
T_{MR} : Temperature melting range
u, $\check{U}$, v, $\check{V}$: Velocity components in x and y directions
x, y : Nondimensional coordinate
$\check{X}$, $\check{Y}$: Dimensionless coordinate

Greek symbols

μ : Dynamic viscid (kg/m $\cdot$ s)
α : Thermal diffusivity (m^2/s)
β : Thermal expansion factor (K^{-1})
Δ : Relative error of computations

δ : Band of phase change
λ : Nondimensional heat capacitance
ρ : Density ($\mathrm{kg/m^3}$)
$\emptyset$: Volume fraction
ψ : Streaming function ($\mathrm{m^2/s}$)
Ψ : Stream function
ν : Kinematic viscosity ($\mathrm{Pa \cdot s}$)
N_v : Dynamic viscosity number

Subscripts

b : Suspension of NEPCM
c : Cold
co : NEPCM core
bf : Base fluid
fu : Fusion property
h : Hot wall
i : Inner
p : NEPCM particle
o : Outer
sh : NEPCM shell

1. Introduction

Phase change material (PCM) exhibits a principal advantage in different scientific research areas due to its substantial latent heat under ~~a~~ slight temperature change. Recently, a developed type of nanofluids comprising nano-encapsulated phase-changing materials (NEPCMs) has been considered. These NEPCMs consist of a shell as wall material and a PCM as a core material. The latter is filled with PCM that can be changed from solid to liquid state and vice versa when it undergoes a desirable temperature of fusion and distributes or sucks a considerable amount of energy due to the potential thermal energy of the phase transition.

Several industries might benefit from using NEPCMs, including thermal energy storage and heat exchangers,[1–4] solar TES,[5,6] construction, food packaging,[7] electronic cooling devices[8] and medical.[9,10] Many engineering implementations are involved to examine the naturally convective heat transference in non-Newtonian fluids with NEPCMs, particularly for thermal energy storage systems, domestic heat pumps and air conditioning systems.[11–13] Different approaches have been used to overcome the little thermal conductivity of PCMs. One of these techniques is to add fins to study the melting process of PCMs in heat storage units, as reported in Refs. 14–19. The results displayed that the transient phase change process is dependent on different parameters such as heat flux, PCM heat capacity and fin dimensions. Another proposed technique is to use several PCMs as in Ref. 20, where they analytically investigated the energy optimization of the solar thermal energy scheme, which includes solar collector and rectangular H_2O storing with slabs containing multiple PCMs.

Using additives such as nanoparticles in PCM can also be considered as another alternative technique to augment heat transfer efficiency. Mettawee and Assassa[21] did several experiments to examine the consequence of adding nanoparticles to paraffin solidification and melting a solar collector. The experiments showed that the time of discharging and charging could be minimized using aluminum particles. Hence, nanoparticle thermal conductance is a key parameter affecting the phase change process. The impact of high thermal conductance nanoparticles on PCM performance is scrutinized by Seeniraj *et al.*[22] They discovered that the existence of nanoparticles in the PCMs amplifies the mixture's heat flux and decreases the system's cumulative energy storage. The incorporation of the compressed natural graphite matrices has been analyzed by Zhong *et al.*[23] It is demonstrated that composite thermal conductance is greater by 28–180 times than pure paraffin. The influence of dispersing nanoparticles on the melting rate with energy/exergy storage in a system of storing latent heat has been mathematically assessed by Jegadheeswaran and Pohekar.[24] It is observed that adding nanoparticles augments the latent heat thermal storage (LHTS) performance. Gopal *et al.*[25] performed a thermodynamic evaluation of PCM integrated with a diesel engine. The thermal efficiency of the system varied in the range of 3.19–34.15%.

Recently, metal foams with high thermal conductivity, such as Nickel, Copper and Aluminum, have been employed for boosting heat transfer in PCMs. Metal foam can be considered a solid porous matrix in which PCMs are dispersed in the voids. Several studies on the effect of PCM-metal are reviewed in the literature. For instance, Ghalambaz *et al.*[26] studied theoretically the exchange of heat in non-Newtonian PCM filled in an enclosed cylindrical geometry. A deformed mesh method is followed in modeling the heat exchange process in PCMs. The results showed that when the power law index declines or the Darcy number rises, the rate of heat transference is boosted in the enclosure, and hence the melting process is enhanced. The Darcy–Brinkman formulation was used by Ghalambaz and Zhang[27] to assess the flow and convective heat transference of PCMs with the metallic foaming filled between two horizontal cylinders (heat sink). The inner surface of annuli is exposed to pulse load, whereas the outer wall is cooled by convection, using the enthalpy porosity model for phase change. The results showed that heat exchange at the hot wall is augmented as the heat sink is covered by phase-changing material. Also, the efficiency of the heat sink increases as the Biot number decreases.

Many researchers have modeled and examined the free convection of nanoparticle suspensions without PCM in various cavities in the absence and presence of a magnetic field effect. Kefayati[28] analyzed the impact of magneto force on the natural convective in an open hollow filled with H_2O–alumina by the lattice Boltzmann method (LBM). It is shown that the heat exchange declines by increasing the strength of the magnetic field. In another study, Kefayati[29] examined the impact of magnetohydrodynamics (MHD) on the convection flowing within a cavity occupied with H_2O–CuO and subjected to the sinusoidal temperature distribution. Their results showed that the magneto force enhanced the role of nanomolecules at moderate Rayleigh quantity ($Ra = 10^5$). However, an adverse impact was seen at $Ra = 10^3$ and 10^4. Also, Kefayati[30] analyzed the effect of heat dissipation of Cobalt-Kerosene on the convective flow in a cavity using the LBM. The results showed that at different Ra's, the heat exchange rate decreases as ferromagnetic particles' fractional size increases. Natural convection of (H_2O–Cu) nanofluid in a porous parallelogram enclosure has been analyzed numerically by Ghalambaz *et al.*,[31] using the early model of Tiwari and Das. The outcomes indicated a decline in heat exchange with the rise of mixture viscosity. Ghalambaz and Sabour[32] conducted a numerical study on the LTNE convection heat and mass transference of nanoliquids in a porous triangular enclosure, using different models of the energy equation. Four-equation Buongiorno's model was used. They reported that the Nusselt number rises with rising Ra in the case of regular fluid. However, less increase was observed for the case of nanofluids. LBM has been employed by Kefayati[33] to analyze the generation of entropy with heat transfer in free convection of non-Newtonian nanoliquids in a cavity, with the impact of magneto force. It is highlighted that growing the consistency indexing deteriorates the rate of heat exchange with zero magnetic force, while with MHD, the boost of consistency indexing amplifies the rate of heat exchange. Kefayati[34] conducted research work in the same procedure as the previous research but in a porous cavity. Considerable decrease in both heat exchange and the generated entropy is observed at a low Darcy number.

Zargartalebi *et al.*[35] studied the laminar convective heat transference in the cavity with a thin inclined porous fin filled by nanoliquid, based on Buongiorno's model. The thermally nonequilibrium state was taken into consideration. The findings showed the augmentation of Nusselt number with rising Prandtl, Rayleigh and Darcy numbers and porosity, but it decreases with the increase of both fin position and thermal conductivity ratio. Kefayati[36] employed the Buongiorno model to study the combined convection of non-Newtonian nanoliquid in a square cavity at a Prandtl quantity of unity. The outcomes demonstrated that the consistency indexing decreases heat and mass transference at the Richardson number of 0.001 and 0.01. An increase in Brownian and thermophoresis motion parameters are found to augment the mass transfer and reduce the heat exchange rate noticeably.

Mehryan *et al.*[37] have used hybrid nanofluids to augment the heat capacity of the working fluids. They dispersed Al_2O_3–Cu–H_2O nanofluids in a porous enclosure. They noticed greater heat exchange in the single nanofluid, and the average Nusselt quantity relates to the nanoparticles' fractional size, as in the examination of Ghalambaz *et al.*[38] The impact of twin layers— a porous medium and a solid wall, on the convective heat exchange and nanofluid flow have been suggested by Tahmasebi *et al.*[39] and also by Mehryan *et al.*[40] Similarly, the outcomes showed a magnified heat exchange rate with rising Rayleigh and Darcy numbers and the ratio of thermal conductivity (porous and solid domain). Recently, many numerical and experimental investigations had studied the effects of hybrid or nanofluids with a porous medium.[41–43]

As previously mentioned, a new type of nanoparticles, namely NEPCMs have been used to boost the heat capacity of heat transfer fluids. The encapsulated method has the advantage of augmentating the heat transfer rate and keeping PCMs from leakage. Within the temperature of fusion of NEPCM, the heat capacitance of the suspension is improved, resulting in the promotion of thermal conductance, which enhances the heat transference as mentioned in Ghalambaz *et al.*,[44] but at the same time, they decrease the buoyancy force and sensible heat capacity which led to heat transfer reduction. When the potential heat of PCM cores upsurges, i.e., as Stefan quantity diminishes, the Nusselt number also rises. The mixed convection heat transference of NEPCM suspension in a saturated porous vertical flatness plate was considered by Ghalambaz *et al.*[45] They deduced that adding NEPCM or lowering the melting temperature of NEPCM augments the rate of heat transference over the flat plate. The natural convection in NEPCM suspension filled in an enclosure with time-periodic hot surface temperature is considered by Hajjar *et al.*[46] It is detected that the heat exchange is augmented by 21% as the fractional size of nanomolecules upsurges from 2.5% to 5%.

The previous research studies showed that substantial efforts have been devoted to dealing with the free convection of Newtonian flows with NEPCMs. However, according to the authors' knowledge, there is no research regarding the free convection of non-Newtonian flows in NEPCM suspensions, which is important for future thermal systems. According to open literature, thisresearch is the first study on the simulation and modeling of the natural convective heat transference of non-Newtonian liquid with NEPCMs in a square enclosure.

2. Problem Formalization

Figure 1 describes the considered problem and its boundary conditions. The geometry is 2D square enclosure of side length L. The left surface is kept at a higher temperature T_h and the right surface is maintained at a colder temperature T_c. The horizontal surfaces are thermally insulated. The content of the enclosure is non-Newtonian fluid and nano-encapsulated PCM. At the fusion dimensionless temperature θ_f, where $0 < \theta_f < 1$, the core of the NEPCM is subjected to phase change.

The phase of the core changes between solid and liquid states when the energy is absorbed or released. In this work, the natural convection of non-Newtonian fluid with NEPCM is considered in which the mixture is assumed regular and settled, non-Newtonian, in thermal equilibrium and no slippage constraints between non-Newtonian fluid and NEPCM. The thermophysical properties are supposed to be constant, but the density changes according to the Boussinesq approach.

Following Refs. 44, 47 and with some modifications, the conservation governing equations can be stated as

$$\frac{\partial u}{\partial x}+\frac{\partial v}{\partial y}=0, \tag{1}$$

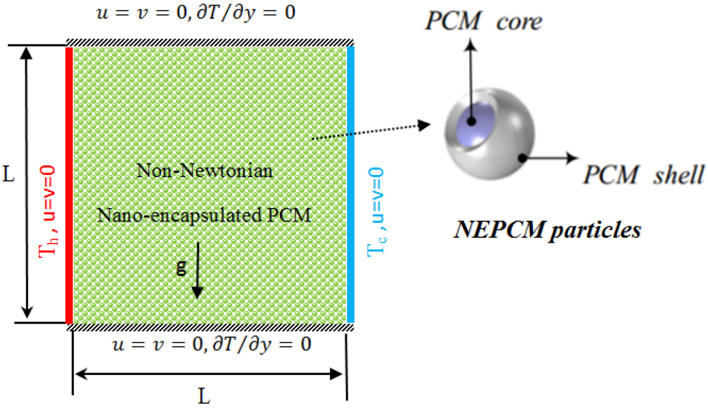

Fig. 1. (Color online) Schematic view of the physical model.

$$\rho_b\left(u\frac{\partial u}{\partial x}+v\frac{\partial u}{\partial y}\right)=-\frac{\partial p}{\partial x}+\left(\frac{\partial \tau_{xx}}{\partial x}+\frac{\partial \tau_{xy}}{\partial y}\right), \tag{2}$$

$$\rho_b\left(u\frac{\partial v}{\partial x}+v\frac{\partial v}{\partial y}\right)=-\frac{\partial p}{\partial y}+\left(\frac{\partial \tau_{xy}}{\partial x}+\frac{\partial \tau_{yy}}{\partial y}\right)+\rho_b g\beta_b(T-T_c), \tag{3}$$

$$(\rho c_p)_b\left(u\frac{\partial T}{\partial x}+v\frac{\partial T}{\partial y}\right)=k_b\left(\frac{\partial^2 T}{\partial x^2}+\frac{\partial^2 T}{\partial y^2}\right). \tag{4}$$

Herein u, v are the speeds in x, y orientations, correspondingly. The pressure and temperature are represented by $p$and T, respectively. The properties of the fluid mixture, like consistency, specific heat, thermal expansion and thermal conductance, are denoted by ρ, c_p, β and k respectively, the symbol of subscript b refers to the suspension bulk properties and g refers to the gravity acceleration.

The non-Newtonian fluid behavior is expressed using the Ostwald–de Waele model, and it is given by Refs. 48 and 49

$$\tau_{ij}=2\mu_{\text{eff}}D_{ij}=\mu_{\text{eff}}\left(\frac{\partial u_i}{\partial x_j}+\frac{\partial u_j}{\partial x_i}\right), \tag{5}$$

where D_{ij} denotes the deformation rate tensor for 2D Cartesian form, while μ_{eff} denotes the effective viscosity for 2D Cartesian form, and it is described by

$$\mu_{\text{eff}}=M\left\{2\left[\left(\frac{\partial u}{\partial x}\right)^2+\left(\frac{\partial v}{\partial y}\right)^2\right]+\left(\frac{\partial v}{\partial x}+\frac{\partial u}{\partial y}\right)^2\right\}^{\left(\frac{n-1}{2}\right)}, \tag{6}$$

where M denotes the factor of consistency and n the indexing of consistency. Thus, $n = 1$ accounts for the Newtonian liquid, while $n > 1$ and $n < 1$ represent dilatant and pseudoplastic fluids, respectively. The thermal and dynamical boundary constraints of thiswork are expressed as

$$\text{Left hot wall } x=0, \quad u=v=0, \quad T=T_h, \tag{7a}$$

$$\text{Right cold wall } x = L, \quad u = v = 0, \quad T = T_c, \tag{7b}$$

$$\text{Bottom adiabatic wall } y = 0, \quad u = v = 0, \quad \frac{\partial T}{\partial y} = 0, \tag{7c}$$

$$\text{Top adiabatic wall } y = L, \quad u = v = 0, \quad \frac{\partial T}{\partial y} = 0. \tag{7d}$$

To transform the dimensional equations (Eqs. (1)–(4)) and the boundary constraints (Eqs. (7a)–(7d)), into dimensionless form, some dimensionless parameters are introduced as follows[33]:

$$\check{X}, \quad \check{Y} = \frac{x, y}{L}, \quad \check{U} = \frac{uL}{\alpha_{\mathrm{bf}}}, \quad \check{V} = \frac{vL}{\alpha_{\mathrm{bf}}}, \quad \check{P} = \frac{pL^2}{\rho_{\mathrm{bf}}\alpha_{\mathrm{bf}}^2}, \quad \theta = \frac{T - T_c}{T_h - T_c}. \tag{8}$$

The dimensionless parameters of Ra (Rayleigh number) and Pr(Prandtl number) can be represented as

$$\mathrm{Ra} = \frac{\rho_{\mathrm{bf}} g \beta_{\mathrm{bf}} (T_h - T_c) L^3}{\alpha_{\mathrm{bf}} \mu_{\mathrm{bf}}}, \quad \mathrm{Pr} = \frac{\mu_{\mathrm{bf}}}{\rho_{\mathrm{bf}} \alpha_{\mathrm{bf}}}. \tag{9}$$

Substituting Eqs. (8), (9) into Eqs. (1)–(5), the following nondimensional equations are attained:

$$\frac{\partial \check{U}}{\partial \check{X}} + \frac{\partial \check{V}}{\partial \check{Y}} = 0, \tag{10}$$

$$\begin{aligned}\left(\frac{\rho_b}{\rho_{\mathrm{bf}}}\right)&\left(\check{U}\frac{\partial \check{U}}{\partial \check{X}} + V\frac{\partial \check{U}}{\partial \check{Y}}\right)\\ &= -\frac{\partial \check{P}}{\partial \check{X}} + \frac{1}{\rho_{bf}\alpha_{bf}}(1 + N_v\emptyset)\left[2\frac{\partial}{\partial \check{X}}\left(\frac{\check{\mu}_{\mathrm{eff}}}{M}\frac{\partial \check{U}}{\partial \check{X}}\right) + \frac{\partial}{\partial \check{Y}}\left(\frac{\check{\mu}_{\mathrm{eff}}}{M}\left(\frac{\partial \check{U}}{\partial \check{Y}} + \frac{\partial \check{V}}{\partial \check{X}}\right)\right)\right],\end{aligned} \tag{11}$$

$$\begin{aligned}\left(\frac{\rho_b}{\rho_{\mathrm{bf}}}\right)&\left(\check{U}\frac{\partial \check{V}}{\partial \check{X}} + V\frac{\partial \check{V}}{\partial \check{Y}}\right)\\ &= -\frac{\partial \check{P}}{\partial \check{Y}} + \frac{1}{\rho_{\mathrm{bf}}\alpha_{\mathrm{bf}}}(1 + N_v\emptyset)\left[2\frac{\partial}{\partial \check{Y}}\left(\frac{\check{\mu}_{\mathrm{eff}}}{M}\frac{\partial \check{V}}{\partial \check{Y}}\right) + \frac{\partial}{\partial \check{X}}\left(\frac{\check{\mu}_{\mathrm{eff}}}{M}\frac{\partial \check{V}}{\partial \check{Y}}\right)\right.\\ &\quad\left. + \frac{\partial}{\partial X}\left(\frac{\check{\mu}_{\mathrm{eff}}}{M}\left(\frac{\partial \check{U}}{\partial \check{Y}} + \frac{\partial \check{V}}{\partial \check{X}}\right)\right)\right] + \mathrm{Pr}\left(\frac{\beta_b}{\beta_{\mathrm{bf}}}\right)\theta,\end{aligned} \tag{12}$$

$$\left(\frac{\rho_b C\check{p}bf}{\rho_{\mathrm{bf}} C_{p_{\mathrm{bf}}}}\right)U\frac{\partial \theta}{\partial \check{X}} + \check{V}\frac{\partial \theta}{\partial \check{Y}} = \frac{K_b}{K_{\mathrm{bf}}}\left(\frac{\partial^2 \theta}{\partial \check{X}^2} + \frac{\partial^2 \theta}{\partial \check{Y}^2}\right), \tag{13}$$

$$\check{\mu}_{\mathrm{eff}} = M\left\{2\left[\left(\frac{\partial \check{U}}{\partial \check{X}}\right)^2 + \left(\frac{\partial \check{V}}{\partial \check{Y}}\right)^2 + \left(\frac{\partial \check{V}}{\partial \check{X}} + \frac{\partial \check{U}}{\partial \check{Y}}\right)^2\right]\right\}^{\left(\frac{n-1}{2}\right)}. \tag{14}$$

The consistency of the combination may be calculated utilizing the consistency of the NEPCM molecules and the density of the conventional fluid,[50,51] and it is given by

$$\rho_b = (1 - \emptyset)\rho_{\mathrm{bf}} + \emptyset\rho_p, \tag{15}$$

where $\emptyset$ refers to the NEPCM volume fraction, ρ expresses the density, and the subscripts b, bf and p refer to the properties of NEPCM, base fluid and NEPCM particles, respectively.

The NEPCM consists of a substance (core) and a cortex (shell). The relation describing the density of the nanofluid is expressed as[44,46]

$$\rho_{\mathrm{na}} = \frac{(1+l)\rho_{\mathrm{co}}\rho_{\mathrm{sh}}}{\rho_{\mathrm{sh}} + l\rho_{\mathrm{co}}}. \tag{16}$$

Subscripts sh and co stand for the shell and core of NEPCM, respectively, whereas l is the weight ratio of the core to the shell, which is about $l \sim 0.447$.[46]

The relation between the ratio of heat capacitance of the conventional liquid and nanofluid on one side and the overall shell and core heat capacity on the other side can be expressed as[50,51]

$$C_{p_{bu}} = \frac{(1-\emptyset)\rho_f C_{p_{\mathrm{bf}}} + \emptyset\rho_p C_{p_p}}{\rho_b}. \tag{17}$$

C_{p_p} is calculated as follows for the procedure with no phase transition:

$$C_{p_p} = \frac{(C_{p_{\mathrm{co}}} + lC_{p_{\mathrm{sh}}})\rho_{\mathrm{co}}\rho_{\mathrm{sh}}}{(l\rho_{\mathrm{co}} + \rho_{\mathrm{sh}})\rho_p}. \tag{18}$$

The specific heat capacitance of the NEPCM molecules is modeled using a sinusoidal pattern that takes into account the latent heat of the core.[44]

The specific heat capacitance of NEPCM depends on both solid and liquid states. Therefore, the specific heat substance (core) is calculated as the mean value of the two states, which is referred to by subscript co and l. Rectangular, triangular or sinusoidal profiles can be utilized to describe the specific heat as it undergoes a phase change process[44,46] and is given by

$$C_{p_{\mathrm{co}}} = C_{p_{\mathrm{co},l}} + \frac{h_{sf}}{T_{\mathrm{MR}}}, \tag{19a}$$

$$C_{p_{\mathrm{co}}} = C_{p_{\mathrm{co},l}} + \left\{\frac{\pi}{2}\left(\frac{h_{sf}}{T_{\mathrm{MR}}} - C_{p_{\mathrm{co},l}}\right)\sin\left(\pi\frac{T-T_o}{T_{\mathrm{MR}}}\right)\right\}, \tag{19b}$$

$$C_{p_{\mathrm{co}}} = C_{p_{\mathrm{co},l}} + 2\left(\frac{h_{fs}}{T_{\mathrm{MR}}^2} - \frac{C_{p_{\mathrm{co},l}}}{T_{\mathrm{MR}}}\right)(T - T_o), \tag{19c}$$

where T_{MR} denotes the temperature range of phase change.

In this study, the triangular profile (Eq. (19b)) is chosen to describe the latent heat of the core, also the following equation is utilized to describe the specific heat capacitance of the PCM:

$$C_{p_{\text{co}}} = C_{p_{\text{co},l}} + \left\{\frac{\pi}{2}\left(\frac{h_{sf}}{T_{\text{MR}}} - C_{p_{\text{co},l}}\right)\sin\left(\pi\frac{T - T_o}{T_{\text{MR}}}\right)\right\}$$
$$\times \begin{cases} 0, & T < T_f - \dfrac{T_{\text{MR}}}{2}, \\ 1, & T_f - T_{\text{MR}} < T < T_f + T_{\text{MR}}/2, \\ 0, & T > T_f + \dfrac{T_{\text{MR}}}{2}. \end{cases} \tag{20}$$

The thermal expansion, conductivity and viscosity of the base fluid can be expressed as follows:

$$\beta_b = (1 - \emptyset)\beta_{\text{bf}} + \emptyset\beta_p, \tag{21}$$

$$\frac{k_b}{k_{\text{bf}}} = 1 + N_c\emptyset, \tag{22}$$

$$\frac{\mu_b}{\mu_{\text{bf}}} = 1 + N_v\emptyset, \tag{23}$$

where N_c and N_v refer to the thermal conductivity and viscosity number, respectively, which vary according to various parameters like size, type and shape of the nanoparticle and the base fluid.

After substituting the above thermophysical properties according to Eqs. (15)–(21) into Eqs. (10)–(13), the following equations are produced:

$$\frac{\partial\check{U}}{\partial\check{X}} + \frac{\partial\check{V}}{\partial\check{Y}} = 0, \tag{24a}$$

$$\left[(1 - \emptyset) + \emptyset\frac{\rho_p}{\rho_{\text{bf}}}\right]\left(\check{U}\frac{\partial\check{U}}{\partial\check{X}} + V\frac{\partial\check{U}}{\partial\check{Y}}\right)$$
$$= -\frac{\partial\check{P}}{\partial\check{X}} + \frac{1}{\rho_{bf}\alpha_{bf}}(1 + N_v\emptyset)\left\{2\frac{\partial}{\partial\check{X}}\left(\frac{\check{\mu}_{\text{eff}}}{M}\frac{\partial\check{U}}{\partial\check{X}}\right) + \frac{\partial}{\partial\check{Y}}\left[\frac{\check{\mu}_{\text{eff}}}{M}\left(\frac{\partial\check{U}}{\partial\check{Y}} + \frac{\partial\check{V}}{\partial\check{X}}\right)\right]\right\}, \tag{24b}$$

$$\left[(1 - \emptyset) + \emptyset\frac{\rho_p}{\rho_{\text{bf}}}\right]\left(\check{U}\frac{\partial\check{V}}{\partial\check{X}} + V\frac{\partial\check{V}}{\partial\check{Y}}\right)$$
$$= -\frac{\partial\check{P}}{\partial\check{Y}} + \frac{1}{\rho_{bf}\alpha_{bf}}(1 + N_v\emptyset)\left\{2\frac{\partial}{\partial\check{Y}}\left(\frac{\check{\mu}_{\text{eff}}}{M}\frac{\partial\check{V}}{\partial\check{Y}}\right) + \frac{\partial}{\partial\check{X}}\left(\frac{\check{\mu}_{\text{eff}}}{M}\frac{\partial\check{V}}{\partial\check{Y}}\right)\right.$$
$$\left. + \frac{\partial}{\partial X}\left[\frac{\check{\mu}_{\text{eff}}}{M}\left(\frac{\partial\check{U}}{\partial\check{Y}} + \frac{\partial\check{V}}{\partial\check{X}}\right)\right]\right\} + \Pr\left[(1 - \emptyset) + \emptyset\frac{\beta_p}{\beta_{\text{bf}}}\right]\theta, \tag{24c}$$

$$\check{U}\frac{\partial\theta}{\partial\check{X}} + \check{V}\frac{\partial\theta}{\partial\check{Y}} = \frac{(1 + N_v\emptyset)}{Cr}\left(\frac{\partial^2\theta}{\partial\check{X}^2} + \frac{\partial^2\theta}{\partial\check{Y}^2}\right). \tag{24d}$$

The dimensionless parameters θ_f, δ and λ are expressed as follows:

$$\theta_f = \frac{T_f - T_c}{T_w - T_c}, \quad \delta = \frac{T_{\text{MR}}}{T_w - T_c}, \quad \lambda = \frac{(C_{p_{\text{co},l}} + lC_{p_{\text{sh}}})\rho_{\text{co}}\rho_{\text{sh}}}{(\rho C_p)_{bf}(\rho_{\text{sh}} + l\rho_{\text{co}})}. \tag{25}$$

Here, θ_f refers to the dimensionless temperature of fusion, δ is the dimensionless melting interval and λ is the utilitarian heat capacitance ratio.

The term C_r which refers to the ratio of heat capacitance of the suspension to the pure liquid is defined as

$$C_r = \frac{C_{p_{bu}}\rho_{bu}}{C_{p_{\text{bf}}}} C_{p_{\text{bf}}} = (1 - \emptyset) + \emptyset\lambda + \frac{\emptyset}{\delta \text{Ste}} f, \tag{26}$$

where the term $\frac{C_{p_{bu}}\rho_{bu}}{C_{p_{\text{bf}}}\rho_{\text{bf}}}$ is calculated utilizing Eqs. (17)–(20).

$$\begin{aligned} \frac{C_{p_{bu}}\rho_{bu}}{C_{p_{\text{bf}}}}\rho_{\text{bf}} &= (1 - \emptyset) + \emptyset \frac{(C_{p_{\text{co},l}} + lC_{p_{\text{sh}}})\rho_{\text{co}}\rho_{\text{sh}}}{C_{p_{\text{bf}}}}(\rho_{\text{sh}} + \rho_{\text{co}})\rho_{\text{bf}} \\ &\quad + \emptyset \frac{T_w - T_c}{T_{\text{MR}}} \left\{ \frac{\pi \rho_{\text{co}}\rho_{\text{sh}}}{2C_{p_{\text{bf}}}(\rho_{\text{sh}} + l\rho_{\text{co}})\rho_{\text{bf}}} \left(\frac{h_{sf} - C_{p_{\text{co},l}}T_{\text{MR}}}{(T_w - T_c)} \right) \right\} f. \end{aligned} \tag{27}$$

In the above expression, f refers to the dimensionless fusion function, and it is defined as

$$f = \frac{\pi}{2}\sin\left(\frac{\pi}{\delta}\left(\theta - \theta_f + \frac{\delta}{2}\right)\right) \begin{cases} 0, & \theta < \theta_f - \frac{\delta}{2}, \\ 1, & \theta_f - \frac{\delta}{2} < \theta < \theta_f + \frac{\delta}{2}, \\ 0, & \theta > \theta_f + \frac{\delta}{2}. \end{cases} \tag{28}$$

In Eq. (27), the term $[(\rho_{\text{co}}\rho_{\text{sh}})(h_{sf} - C_{p_{\text{co},l}}T_{\text{MR}})]/[(T_w - T_c)(C_{p_{\text{bf}}}(\rho_{\text{sh}} + l\rho_{\text{co}})\rho_{\text{bf}})]$ signifies the pattern of latent heat and plausible heat. T_{MR} specifies the intermission temperature of the phase changing, which is a minor period. Furthermore, the sensible heat, $C_{p_{\text{co},l}}$, is quite tiny in comparison with the latent heat. As a result, the phrase of $C_{p_{\text{co},l}}T_{\text{MR}}$ may be ignored, and the Stefan value can be inserted as standard.

Ste stands for the Stefan number and is defined as

$$\text{Ste} = \frac{(\rho C_p)_{\text{bf}}(T_w - T_c)(\rho_{\text{sh}} + l\rho_{\text{co}})}{h_{sf}\rho_{\text{co}}\rho_{\text{sh}}}. \tag{29}$$

The scaled form of the boundary conditions is obtained as

$$\text{Left hot wall } \check{X} = 0, \quad \check{U} = \check{V} = 0, \quad \theta = 1 \tag{30a}$$

$$\text{Right cold wall } \check{X} = 1, \quad \check{U} = \check{V} = 0, \quad \theta = 0, \tag{30b}$$

$$\text{Bottom adiabatic wall } \check{Y} = 0, \quad \check{U} = \check{V} = 0, \quad \frac{\partial \theta}{\partial \check{Y}} = 0, \tag{30c}$$

$$\text{Top adiabatic wall } \check{Y} = 1, \quad \check{U} = \check{V} = 0, \quad \frac{\partial \theta}{\partial \check{Y}} = 0. \tag{30d}$$

The heat transference rate is defined by Nusselt quantity (Nu) alongside the cold and hot edges, which are, respectively, expressed as

$$\mathrm{Nu}_L = -\frac{k_b}{k_{\mathrm{bf}}}\frac{\partial \theta}{\partial X}\bigg|_{X=0} \quad \text{(Hot wall)}, \tag{31a}$$

$$\mathrm{Nu}_L = -\frac{k_b}{k_{\mathrm{bf}}}\frac{\partial \theta}{\partial X}\bigg|_{X=L} \quad \text{(Cold wall)}. \tag{31b}$$

Nusselt number can be written in terms of the thermal conductivity ratio as

$$\mathrm{Nu}_L = -(1 + N_c\emptyset)\frac{\partial \theta}{\partial X}\bigg|_{X=0} \quad \text{(Hot Wall)}, \tag{32a}$$

$$\mathrm{Nu}_L = -(1 + N_c\emptyset)\frac{\partial \theta}{\partial X}\bigg|_{X=L} \quad \text{(Cold Wall)}. \tag{32b}$$

The average Nu is defined as

$$\mathrm{Nu}_{\mathrm{ave}} = -(1 + N_c\emptyset)\int_0^1 \frac{\partial \theta}{\partial X}\bigg|_{X=L} dy. \tag{33}$$

The average Nu along the cold and hot walls is equal under the condition of a steady state; therefore, it is computed only along the hot wall.

3. Numerical Methodology, Grid Independence and Verification

The FEM based on the Galerkin approach has been implemented to solve the dimensionless equations (Eqs. (10)–(13)). Computational domain with discretization is created, where a two-dimensional finite element mapped mesh is used. A nonuniform distribution mapped mesh with a refined mesh near the enclosure wall is shown in Fig. 2.

The number of divisions of the walls is 150 × 150 with a stretching ratio of 10. The equation of continuity (Eq. (10)) is employed as a constraint for mass accumulation, and this constraint can be used to discover the distribution of pressure. To resolve the dimensionless momentum and energy equations (11)–(13), utilizing the penalty approach anywhere, the term of pressure (P) is discarded by a penalty approach (γ) and the continuity equation (Eq. (10)) is expressed as

$$P = -\gamma\left(\frac{\partial \check{U}}{\partial \check{X}} + \frac{\partial \check{V}}{\partial \check{Y}}\right). \tag{34}$$

A large value of error parameters ($\gamma = 10^7$) is applied to the continuity equation. Therefore, the momentum equation becomes

$$\begin{aligned}\left(\check{U}\frac{\partial \check{U}}{\partial \check{X}} + \check{V}\frac{\partial \check{U}}{\partial \check{Y}}\right) &= \gamma\frac{\partial}{\partial \check{X}}\left(\frac{\partial \check{U}}{\partial \check{X}} + \frac{\partial \check{V}}{\partial \check{Y}}\right) + -\frac{\partial \check{P}}{\partial \check{X}} + \frac{1}{\rho_{bf}\alpha_{bf}}(1 + N_v\emptyset)\\ &\quad\times\left[2\frac{\partial}{\partial \check{X}}\left(\frac{\check{\mu}_{\mathrm{eff}}}{M}\frac{\partial \check{U}}{\partial \check{X}}\right) + \frac{\partial}{\partial \check{Y}}\left(\frac{\check{\mu}_{\mathrm{eff}}}{M}\left(\frac{\partial \check{U}}{\partial \check{Y}} + \frac{\partial \check{V}}{\partial \check{X}}\right)\right)\right],\end{aligned} \tag{35}$$

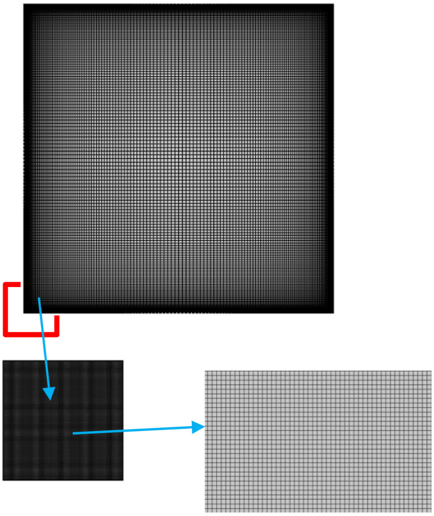

Fig. 2. (Color online) The employed grid (150 × 150) with a stretching ratio of 10.

$$\left(\check{U}\frac{\partial\check{V}}{\partial\check{X}}+V\frac{\partial\check{V}}{\partial\check{Y}}\right)=\gamma\frac{\partial}{\partial\check{Y}}\left(\frac{\partial\check{U}}{\partial\check{X}}+\frac{\partial\check{V}}{\partial\check{Y}}\right)+-\frac{\partial\check{P}}{\partial\check{X}}+\frac{1}{\rho_{bf}\alpha_{bf}}(1+N_v\emptyset)$$
$$\times\left[2\frac{\partial}{\partial\check{X}}\left(\frac{\check{\mu}_{\text{eff}}}{M}\frac{\partial\check{U}}{\partial\check{X}}\right)+\frac{\partial}{\partial\check{Y}}\left(\frac{\check{\mu}_{\text{eff}}}{M}\left(\frac{\partial\check{U}}{\partial\check{Y}}+\frac{\partial\check{V}}{\partial\check{X}}\right)\right)\right]+\Pr\theta. \tag{36}$$

The governing equations employ the weak formulation to produce the following basic set. $[\Pi_I]_{I=1}^{N}$ is used to extract the velocity components (X and Y directions), pressure equation and dimensionless temperature.

$$\begin{aligned}\check{U}&\approx\sum_{I=1}^{N}\check{U}_I\Pi_I(\check{X},\check{Y}), &\check{V}&\approx\sum_{I=1}^{N}\check{V}_I\Pi_I(\check{X},\check{Y}),\\ \check{P}&\approx\sum_{I=1}^{N}\check{P}_I\Pi_I(\check{X},\check{Y}), &\theta&\approx\sum_{I=1}^{N}\theta_I\Pi_I.\end{aligned}\tag{37}$$

To discover the integral of the residual equations, the biquadratic Gaussian of second-order precision is used. Newton's approach, retaining a parallel sparse direct solver (PARADISO) is employed to resolve the residual equation iteratively.

The accuracy of iteration was repeated until the error reached (10^{-5}) with (0.8) Newton's damping factor. The specific information of the used numerical procedure, restriction of the continuity equation with the penalty method, and time step with the correctness of the solution can be found in Refs. 52–55.

Various mesh sizes are examined to ensure high precision in the results as well as short-time computations. Therefore, the average Nusselt quantity along the hot plate and the minimum stream function values are chosen to achieve the adequate grid size, as seen in Table 1 with case details. The mesh study size of 150 × 150 expressed high accuracy and is adequate to obtain accurate numerical outcomes.

Table 1. Effect of grid size on the average Nu for $\mathrm{Ra} = 10^5$, $\delta = 0.05$, $\mathrm{Ste} = 0.2$, $N_c = 23.8$, $N_v = 12.5$, $\lambda = 0.4$, and $\frac{\rho_p}{\rho_f} = 0.75$, $\theta_f = 0.2$ and $n = 0.6$.

Grid	Average Nu	Error (%)	$\psi_{\min}$	Error (%)
100×100	8.7530	—	-0.057257	—
150×150	8.7569	0.044	-0.057269	0.02
200×200	8.7562	-0.008	-0.057276	0.012
250×250	8.7568	0.006	-0.057279	0.0052
300×300	8.7570	0.002	-0.057280	0.0017

Table 2. Comparison of average Nu of this study with those reported by Kefayati[47] at $\mathrm{Ra} = 10^4$.

n	Present study	Kefayati[47]	Error (%)
0.5	2.9102	2.91	-0.006
0.7	2.5368	2.53	-0.268
1	2.2374	2.23	-0.33
1.3	2.0746	2.07	-0.22
1.5	2.0031	2	-0.155

The current code is checked with a recently available paper on free convective heat transfer of non-Newtonian molten polymer by FDLBM and sinusoidal heated boundary condition (Ref. 47) (Table 2). As depicted in Fig. 3, the comparison showed good consistency, so the present code can qualify for our study's numerical task.

4. Results and Discussion

The problem is investigated according to the parameters: nanoparticles volume fraction ($0 < \emptyset < 0.05$), Stefan number ($\mathrm{Ste} = 0.2, 0.313$ and 0.5), heat capacitance ratio (λ) is about (0.4) and the temperature of fusion of the NEPCM core (θ_f) in the area between the cold surface temperature and hot surface temperature ($0 < \theta_f < 1$). The density ratio (ρ_P/ρ_f) is adopted ($0.7 < \rho_P/\rho_f \leq 0.9$) as the PCMs in the core are lighter than non-Newtonian base fluid, and the polymethyl-methacrylate (PMMA) shell is heavier than non-Newtonian normal liquid.

It must be shown that the zero values of the viscosity number (N_v) and conductivity number (N_c) are not applicable for nanofluid, so the values of N_v and N_c are selected as ($N_v = 12.5$) and ($N_c = 23.8$) although larger values are possible. Since the NEPCM volume fraction is low, the coefficient of thermal expansion (β_P) of the solid molecules is remarkably lesser compared to that of the non-Newtonian normal liquids. Hence, the term ($\emptyset * \beta_P/\beta_f$) is assumed to be equal to 0, i.e., it is neglected. The non-Newtonian Prandtl quantity is selected as equal to 6.4. Rayleigh's number range is considered as ($10^4 - 10^6$), minimum Ra values mean the conduction heat transfer regime, while greater Ra means the convection-leading heat transference regime. Also, the value of the dimensionless band of the phase change (δ) is fixed at 0.05.

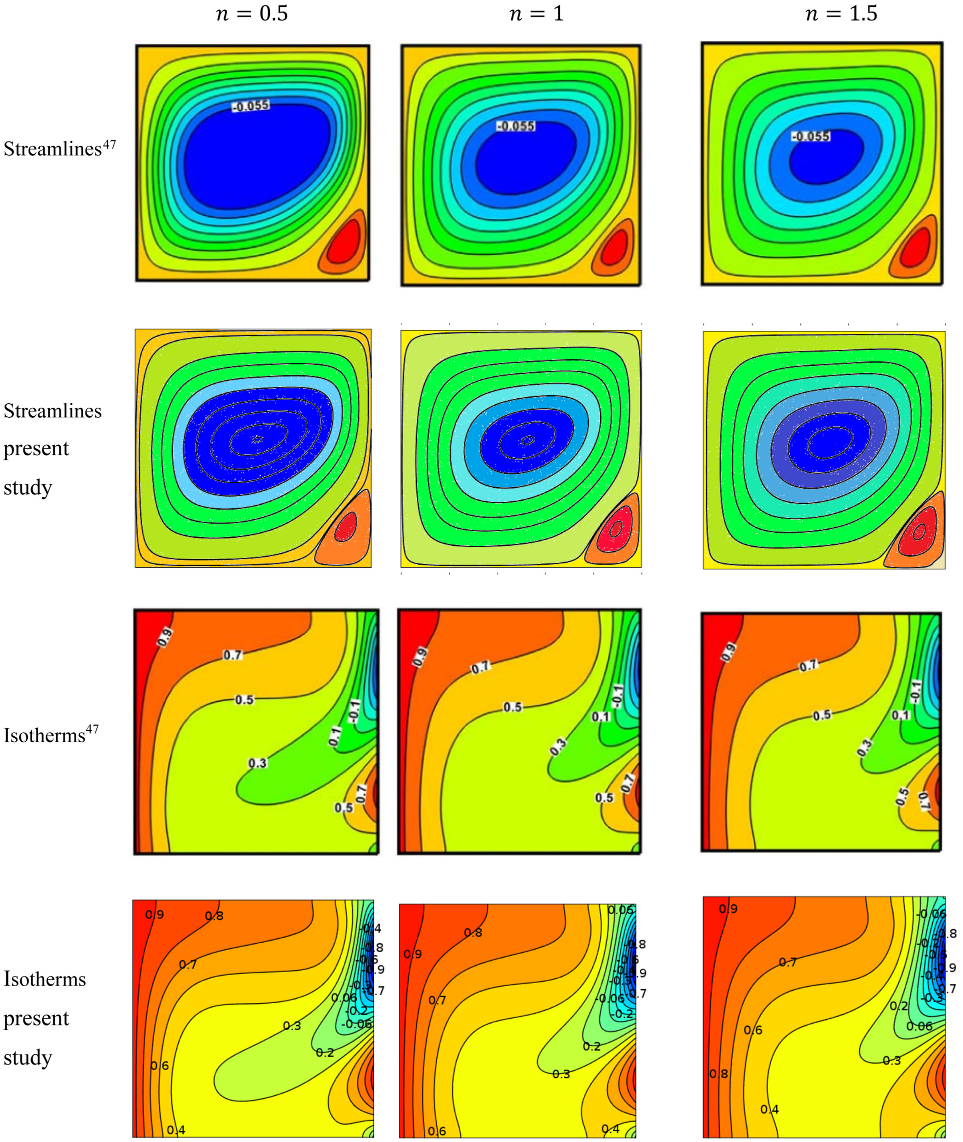

Fig. 3. (Color online) Comparison of streamlines and isotherms from this work with those reported by Kefayati[47] at $\mathrm{Ra} = 10^4$.

Figure 4 shows the power law index (n) impact on isotherms, stream functions and the ratio of heat capacity (C_r) of the suspension to the base for $\theta_f = 0.2$, $\emptyset = 0.05$, $\mathrm{Ste} = 0.2$, $\rho_P/\rho_f = 0.75$ and $\mathrm{Ra} = 10^5$. It is seen that, as n rises from $n = 0.6$ to 1.4, the temperature boundary thickening decreases, and therefore the gradient of temperature reduces, which deteriorates the heat exchange. The isotherm line value of 0.85 can show the impact of n on isotherms, the distance between the

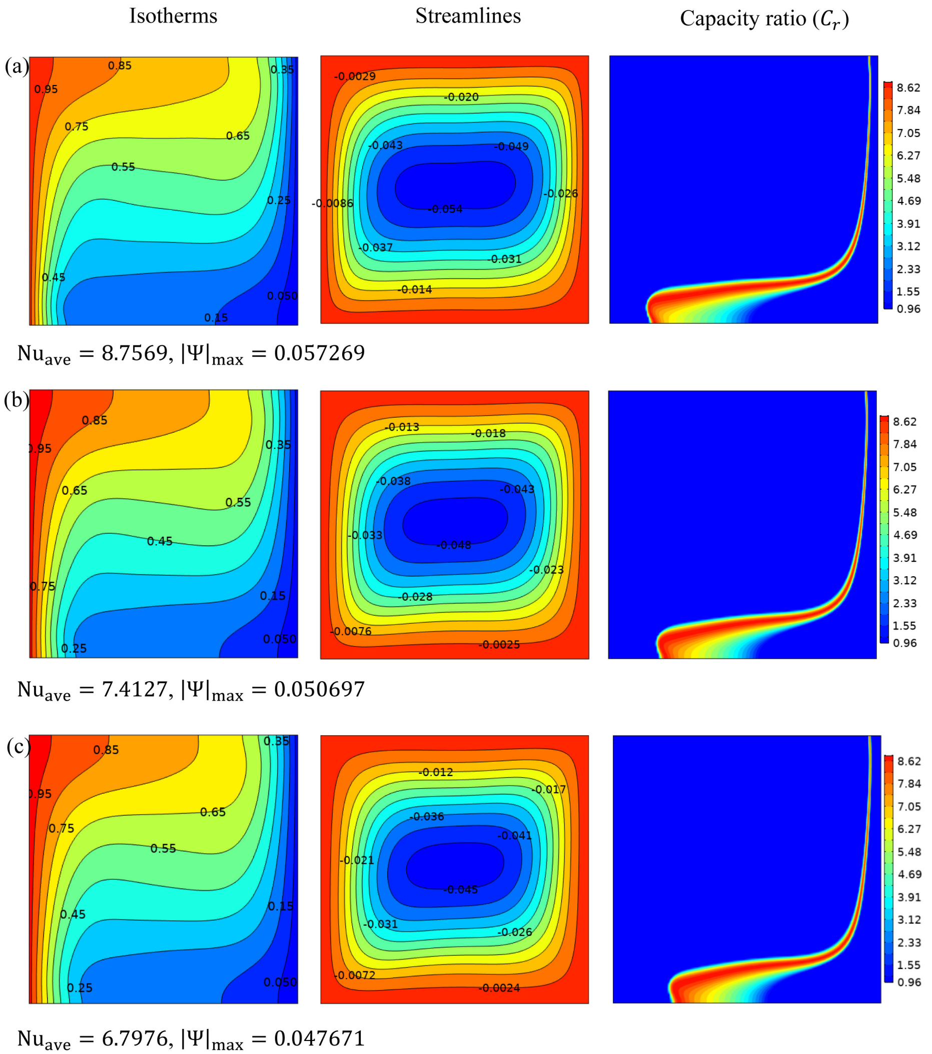

Fig. 4. (Color online) Isotherms (left), streamlines (middle) and heat capacity ratio (C_r) contour maps (right) for (a) $n = 0.6$, (b) $n = 1$ and (c) $n = 1.4$ at $\emptyset = 0.05$, $\mathrm{Ste} = 0.2$, $\frac{\rho_p}{\rho_f} = 0.75$, $\mathrm{Ra} = 10^5$ and $\theta_f = 0.2$.

isotherm value of 0.85 and the hot wall decreases as n increases. Thus, the convective regime becomes less significant at higher power index values. Also, it is shown that the nanofluid inside the cavity moves up along the right wall and flows down along the left wall. Therefore, a single clockwise cell is formed within the cavity. Also, the upsurge in n primes to the deterioration in the streaming function amounts, which clearly specifies that the buoyancy impact becomes less important as n increases. For example, for $n = 0.6$ and $n = 1.4$, the maximum stream function values are $\Psi = 0.057269$ and $\Psi = 0.047671$, respectively. A similar attitude is observed for the maximum value of Nusselt quantity $\mathrm{Nu_{ave}}$. It can be seen that the isotherms at the three values of n look approximately parallel to the adiabatic walls. The nanofluid flow up along the hot side, which induces a single-vortex spinning by flow down alongside the cold edge that is reduced as n goes higher, which is the same trend for $\mathrm{Nu}_{\mathrm{ave}}$.

In the same Fig. 4, the impression of n on the ratio of heat capacity (C_r) is shown. For all n's, the red area illustrates the phase change zone, i.e., the nanoparticles undergo phase change inside the nanocapsule, and the shape becomes a stripe around the constant temperature lines of fusion. In contrast, outside the fusion region, the heat capacity ratio values remain almost constant at $(C_r = 0.96)$ near the wall, and the shape becomes very thin due to high-temperature gradients. However, the shape gets broad near the bottom wall at the center, where the temperature gradients are smooth. When the fusion temperature varies from $\theta_f = 0.2$ to $\theta_f = 0.5$, as shown in Fig. 5, the red area C_r contours in which the core undergoes phase changing, i.e., higher temperature gradients near both the hot and cold surfaces, leads to thinning of the phase change regime, whilst it goes wider at the core of the enclosure because of low-temperature gradients. It can be seen that the expansion of isothermal lines at the base of the enclosure toward the hot surface is widespread as the values of the isotherms are identical to the fusion temperature (θ_f), i.e., the phase change area is moved to the bottom of the hot surface as the temperature of fusion increases. Moreover, it is evident the alteration of the fusion temperature distorts the streamlines and reduces the strength of the flow inside the cavity.

The PCM nanoparticles absorb heat from a heated region and release it to cold regions according to the model explained in Eq. (28). Such a phenomenon can be observed in the C_r contour maps of Figs. 4 and 5. Thus, the phase change of NEPCM liquid is fully coupled to the flow and heat transfer through the governing equations. The final shape of C_r contour maps is due to the nonlinear effects of the natural convection heat transfer and thermal diffusion. According to the isotherm maps, the phase change area is placed around the isotherms, θ_f, which agrees with Eq. (28).

The local Nusselt number $\mathrm{Nu}_{\mathrm{loc}}$ at both cold and hot surfaces for different n is shown in Fig. 6 for $\theta_f = 0.2$ and $\theta_f = 0.5$, $\emptyset = 0.0$, $\frac{\rho_p}{\rho_f} = 0.75$, $\mathrm{Ste} = 0.2$, $N_v = 12.5$, $N_c = 23.8$, $\delta = 0.05$, $\lambda = 0.333$ and $\mathrm{Ra} = 10^5$. It can be shown that due to the fusion temperature values, the $\mathrm{Nu}_{\mathrm{ave}}$ increases significantly as the behavior of the fluid changes from shear thickening $(n > 1)$ to shear thinning $(n < 1)$ along the hot and cold walls. This implies that the convective heat transfer becomes important with the decrease of n. In addition, it is recorded that changing the fusion temperature from $\theta_f = 0.2$ to $\theta_f = 0.5$ has a marginal impact on $\mathrm{Nu}_{\mathrm{ave}}$ near the upper (hot) and along the cold walls. However, $\mathrm{Nu}_{\mathrm{ave}}$ increases significantly with the boosting of the fusion temperature at the bottom wall. As discussed before, the phase change in the NEPCM occurs around isotherms that have nearly the same value as the fusion temperature. In addition, Figs. 4 and 5 have shown that the isotherms in the cavity are slightly impacted by the distinction in the blend temperature for the considered n values. It can be inferred that the rise in the temperature of fusion pushes the phase change in the nanocapsule towards the bottom wall, where $\mathrm{Nu}_{\mathrm{ave}}$ amounts show a significant increase. Also, the isothermal lines are at a distance from the upper part of

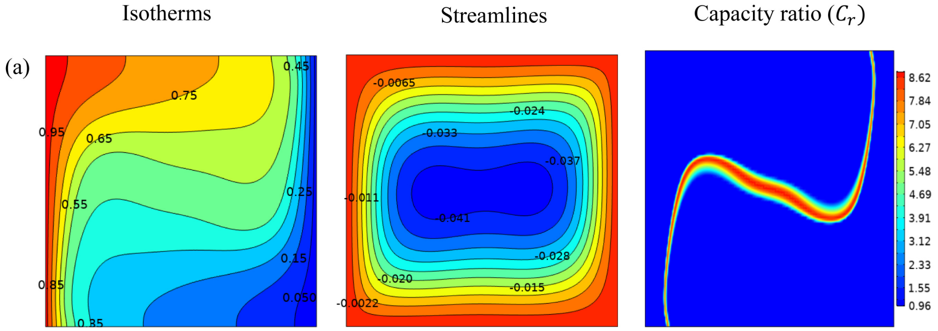

$\mathrm{Nu}_{\mathrm{ave}} = 8.7326$, $|\Psi|_{\max} = 0.043427$

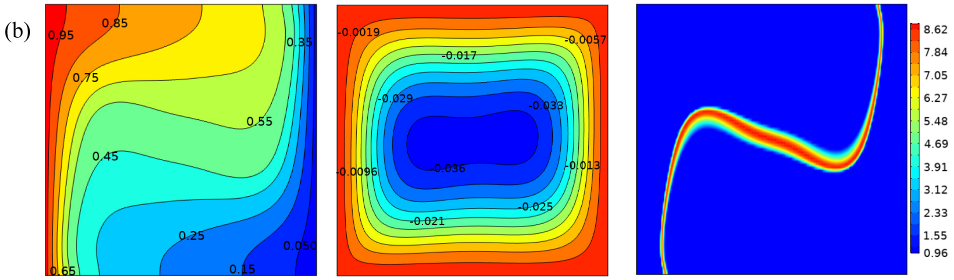

$\mathrm{Nu}_{\mathrm{ave}} = 7.5898$, $|\Psi|_{\max} = 0.038266$

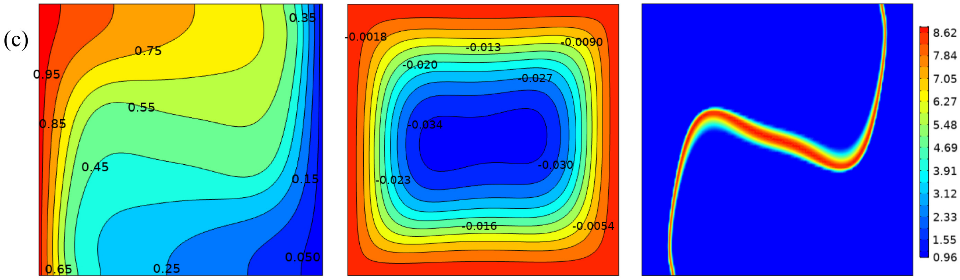

$\mathrm{Nu}_{\mathrm{ave}} = 7.0719$, $|\Psi|_{\max} = 0.035837$

Fig. 5. (Color online) Isotherms (left), streamlines (middle) and heat capacity ratio (C_r) contour maps (right) for (a) $n = 0.6$, (b) $n = 1$ and (c) $n = 1.4$ at $\emptyset = 0.0, \mathrm{Ste} = 0.2$, $\frac{\rho_p}{\rho_f} = 0.75$, $\mathrm{Ra} = 10^5$ and $\theta_f = 0.5$.

the hotness surface, so the profiles of $\mathrm{Nu}_{\mathrm{loc}}$ at the top of the hot surface overlapirrespective of θ_f.

Figures 7(a) and 7(b) illustrate the impact of Stefan's number on $\mathrm{Nu}_{\mathrm{ave}}$ for two values of Ra ($\mathrm{Ra} = 10^4 - 10^5$). It is noted that the mean Nu increments as the Stefan number decreases. This is referred to as the augmentation of the PCM's latent heat at the cavity core. For $\mathrm{Ra} = 10^4$, the maximum average Nu can be observed at a temperature of fusion of $\theta_f = 0.5$, as shown in Figs. 4 and 5. The center of the enclosure behaves like a regime of phase change close to the cold and hot regions.

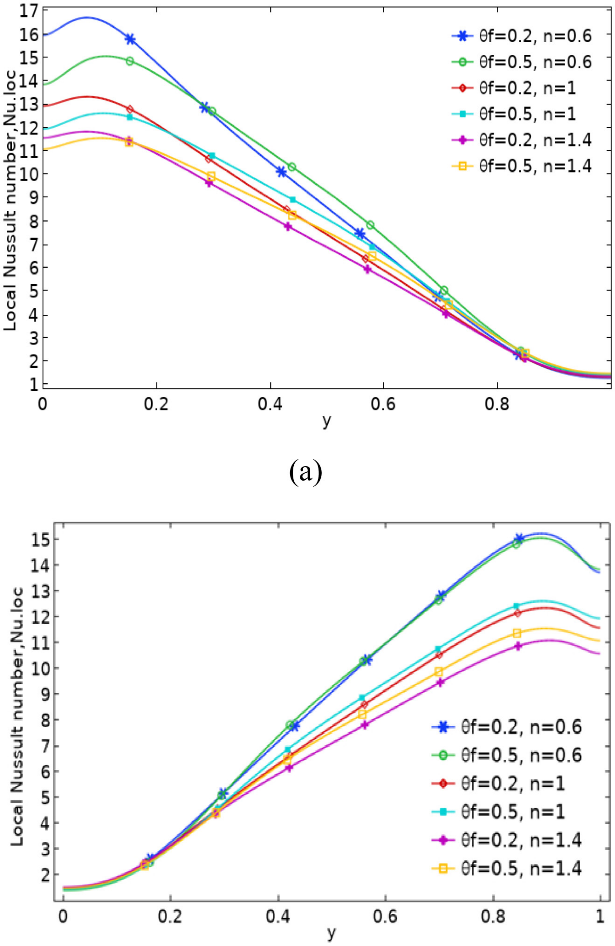

(a)

(b)

Fig. 6. (Color online) Variation of local Nu for (a) hot wall and (b) cold wall when $\theta_f = 0.2, 0.5$, $n = 0.6$, 1, 1.4, $\emptyset = 0.05$, $\frac{\rho_p}{\rho_f} = 0.75$, Ste $= 0.2$, $N_c = 23.8$, $N_v = 12.5$, $\lambda = 0.333$, $\delta = 0.05$ and Ra $= 10^5$.

Thus, the average Nusselt number is maximal in these regions. As Ra increases, the average Nu increases, as seen in Fig. 7(b), indicating that the heat transference rate is a function of temperature θ_f, with uniform behavior at $\theta_f = 0.5$. However, the lowest average Nu is obtained in the range of $0.25 < \theta_f < 0.75$, and the maximum average Nu is recorded at $\theta_f = 0.25$ and 0.75.

Figure 8 demonstrates the average Nu variation with Ra as a function of n at $\emptyset = 0.05$, $N_c = 23.8$, Ste $= 0.2$, $\lambda = 0.33$, $N_v = 12.5$, $\delta = 0.05$, $\theta_f = 0.2$ and $\frac{\rho_p}{\rho_f} = 0.75$. In fact, n describing the stress–strain relation is supposed to vary from low shear thinning fluids ($n = 0.6$) to high shear-thickening fluids ($n = 1.4$), where $n = 1$, $n < 1$ and $n > 1$ represent the Newtonian fluid, the shear thinning or

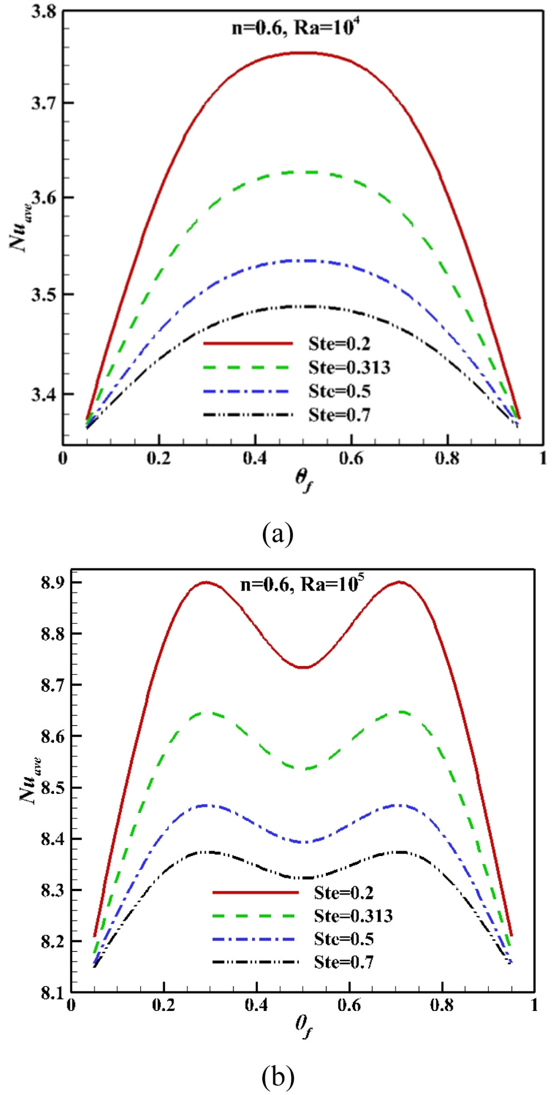

(a)

(b)

Fig. 7. (Color online) Variation of average Nu with nondimensional fusion temperature (θ_f) for various Stefan numbers at $\frac{\rho_p}{\rho_f} = 0.75$, Ste $= 0.2$, $N_c = 23.8$, $N_v = 12.5$, $\lambda = 0.333$, $\emptyset = 0.05$ and $\delta = 0.05$ for (a) $\mathrm{Ra} = 10^4$ and (b) $\mathrm{Ra} = 10^5$.

pseudoplastic fluid (i.e., viscosity declines with increasing the strain rate) and the shear thickening or dilatant fluid (i.e., viscosity increases with increasing the strain rate), respectively. The result exhibits that for $\mathrm{Ra} \leq 10^4$, n has no impression on the $\mathrm{Nu}_{\mathrm{avg}}$. This indicates that a power law index has an insignificant outcome on the enclosure conducting heat exchanging efficacy. However, for $10^4 \leq \mathrm{Ra} \leq 10^6$, the power law index shows a significant effect on the $\mathrm{Nu}_{\mathrm{ave}}$. When n alters from $n = 0.6$ to $n = 1.4$, the maximum $\mathrm{Nu}_{\mathrm{ave}}$ is reduced by almost 23% and 34% at $\mathrm{Ra} = 10^5$ and

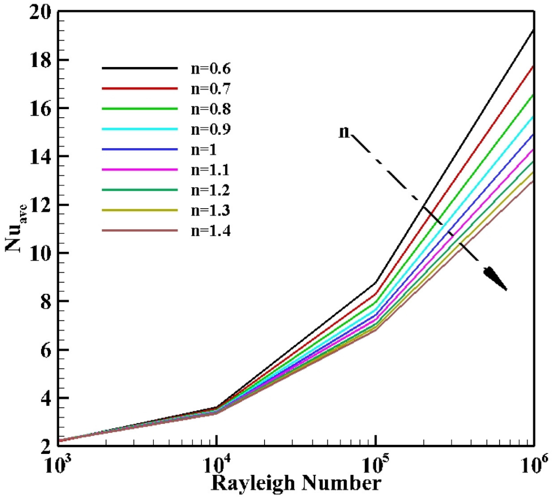

Fig. 8. (Color online) The average Nu versus Ra at different power law indexes $\emptyset = 0.05$, $\mathrm{Ste} = 0.2$, $N_c = 23.8$, $N_v = 12.5$, $\lambda = 0.333$, $\delta = 0.05$, $\theta_f = 0.2$ and $\frac{\rho_p}{\rho_f} = 0.75$.

$\mathrm{Ra} = 10^6$, respectively. All consequences specify that the friction forces among contiguous layers of liquid are higher in the case of shear-thinning liquids than in shear-thinning and even Newtonian liquids. Consequently, the convective influence increases by reducing the power law indexing amounts. Moreover, it is seen that regardless of n, the heat exchange is enhanced with the boost of Ra.

The impact of n and the NEPCM volume fraction on $\mathrm{Nu_{ave}}$ is illustrated in Fig. 9. It is noticed that for all values of n, the heat transfer augments like-linear with the ϕ due to the enhancement of nanofluid thermal conductivity. As discussed previously, when $n = 1$ and according to Fig. 9, the volume fraction of the NEPCM is reduced. $\mathrm{Nu_{ave}}$ decreases considerably when n varies from 0.6 to 1.4 since the numbers of viscosity ratio and the conductivity ratio are collected as $N_c = 23.8$ and $N_v = 12.5$, and hence the nanofluid is considered a dilute suspension ($\emptyset < 0.05$). It can be deduced, hence, that the decrease of NEPCM volume fraction increases the surface velocity at the surface which reduces the dynamic viscosity, the boundary layer thickness and temperature gradient, which lead to a decrease in the average Nu, and consequently decreases the rate of heat transfer.

Table 3 depicts the impact of the average Nu and minimum value of streamlines on different nondimensional variables such as Ste, θ_f, λ, (ρ_P/ρ_f), N_c, N_v and n. It can be shown that the effect of these variables on the average Nu is nonmonotonic. Therefore, the effect of variation of these parameters is also investigated. The increase of N_c and λ increases the average Nusselt number. However, it has an insignificant effect on the minimum streamline values. Also, the increase of N_v and Ste decreases the average Nu whereas the density ratio variation (ρ_P/ρ_f) has a negligible effect on the average Nu. The rise of (θ_f) augments the average Nu. However, it can be seen that the results obtained from Figs. 6(a) and 6(b) on the effect of (θ_f) and the

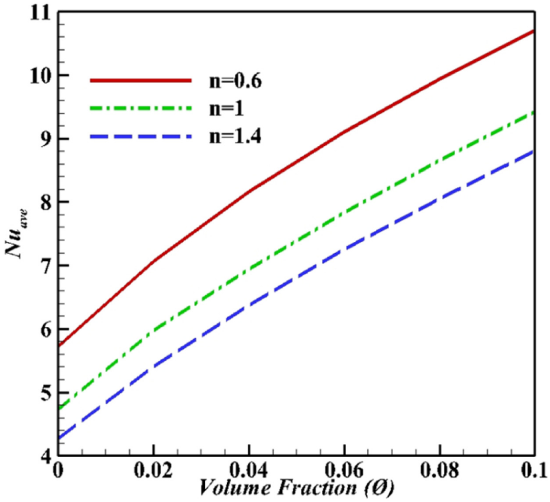

Fig. 9. (Color online) The average Nu with $\emptyset$ for various values of n, $\mathrm{Ste} = 0.313$, $N_c = 23.8$, $N_v = 12.5$, $\lambda = 0.4$, $\delta = 0.05$, $\theta_f = 0.3, \frac{\rho_p}{\rho_f} = 0.9$, $\mathrm{Ra} = 10^5$.

Table 3. Influence of various nondimensional parameters on the average Nu at $\mathrm{Ra} = 10^5$.

Ste	θ_f	λ	ρ_p/ρ_f	N_c	N_v	n	Nu	$\psi_{\min}$
0.313	0.3	0.4	0.9	3	3	0.6	6.2645	−0.040277
0.313	0.3	0.4	0.9	3	6	0.6	5.9455	−0.038309
0.313	0.3	0.4	0.9	6	3	0.6	6.8573	−0.043997
0.313	0.3	0.4	0.9	6	6	0.6	6.5083	−0.041846
0.313	0.3	0.4	0.7	3	3	0.6	6.2647	−0.040284
0.313	0.3	0.3	0.9	3	3	0.6	6.2578	−0.040412
0.313	0.2	0.4	0.7	3	3	0.6	6.2253	−0.042470
0.313	0.1	0.4	0.9	3	3	0.6	6.0512	−0.043473
0.2	0.3	0.4	0.9	3	3	0.6	6.4316	−0.038826
0.5	0.3	0.4	0.9	3	3	0.6	6.1452	−0.041442
0.313	0.3	0.4	0.9	3	6	1	5.0854	−0.032039
0.313	0.3	0.4	0.9	3	6	1.4	4.6898	−0.034003
0.313	0.3	0.4	0.9	23.8	12.5	0.6	8.6490	−0.055232

results presented in Table 3 are consistent with those of Fig. 7(b) and confirm that the Nu is a function of θ_f and the trend will be changed for $\theta_f > 0.5$. The impact of n is shown in Figs. 8 and 9 and shows good agreement with the results of Table 3 at $N_c = 23.8$ and $N_v = 12.5$. It can be shown that when the fluid becomes pseudoplastic $n = 0.6$, the value of $\mathrm{Nu}_{\mathrm{ave}}$ is enhanced.

5. Conclusions

In this paper, free convection of non-Newtonian liquids of NEPCM suspensions enclosed by square boundaries is studied numerically. Throughout, a careful analysis of the effect of NEPCMs on improving the thermal performance of the convective flow in traditional fluids is done, the following main findings are pointed out:

(1) The dispersion of NEPCMs in the standard liquid may cause an upsurge in the heat capacity of a mixture and improve its thermal conductivity at the fusion temperature. On the other hand, NEPCMs may have a negative impression of the heat transference due to a decrease in buoyancy forces and sensible heat capacity and an upsurge in the dynamical viscid.
(2) As the Stefan number declines (i.e., the latent heat of PCM increases), the average Nu increases in the enclosure.
(3) Rising the power law index slows down the convective flow, which diminishes the gradient of temperature and hence the average Nu of the cavity.
(4) The average Nu is phase change temperature-dependent. The heat transference is improved as the fusion temperature becomes close to the hot or cold surface temperature. Higher enhancement is observed as the fusion temperature gets deviated from the wall temperature, particularly in the range of $0.25 < \theta_f < 0.75$.
(5) For the considered power law indices, the boost in the rate of heat transfer is almost linear with the solid fractional size. A higher average Nu is obtained with the shear-thinning fluid. Gradual increase of non-Newtonian power index (n) from the notable shear thinning ($n = 0.6$) to significant shear thickening ($n = 1.4$) monastically reduces the average Nusselt number.

The FEM could be applied to a variety of physical and technical challenges in the future.[56–70]

Acknowledgment

This research of Mohammad Ghalambaz was supported by the Tomsk State University Development Program (Priority 2030).

References

1. S. L. Tariq *et al.*, *Appl. Therm. Eng.* **176**, 115305 (2020).
2. J. M. Khodadadi, L. Fan and H. Babaei, *Renew. Sustain. Energy Rev.* **24**, 418 (2013).
3. M. A. Kibria *et al.*, *Energy Convers. Manage.* **95**, 69 (2015).
4. K. Kant *et al.*, *Sol. Energy* **146**, 453 (2017).
5. D. K. Singh *et al.*, *Appl. Therm. Eng.* **110**, 564 (2017).
6. P. Sarathkumar *et al.*, *Mater. Today Proc.* **4**, 2314 (2017).
7. J. H. Johnston *et al.*, *Curr. Appl. Phys.* **8**, 508 (2008).
8. S. I. Hussain *et al.*, *Energy Build.* **143**, 17 (2017).
9. A. R. Hirst *et al.*, *Angew. Chem., Int. Ed.* **47**, 8002 (2008).
10. M. A. Seo *et al.*, *Nat. Photonics* **3**, 152 (2009).
11. K. Pielichowska and K. Pielichowski, *Prog. Mater. Sci.* **65**, 67 (2014).
12. P. Moreno *et al.*, *Renew. Sustain. Energy Rev.* **39**, 1 (2014).
13. A. Jahanbakhshi, A. A. Nadooshan and M. Bayareh, *J. Therm. Anal. Calorim.* **133**, 1407 (2018).

14. V. Shatikian, G. Ziskind and R. Letan, *Int. J. Heat Mass Transf.* **48**, 3689 (2005).
15. V. Shatikian, G. Ziskind and R. Letan, *Int. J. Heat Mass Transf.* **51**, 1488 (2008).
16. M. Sheikholeslami, *J. Mol. Liq.* **259**, 424 (2018).
17. N. Bondareva and M. Sheremet, Natural convection melting of nano-enhanced phase change material in a cavity with finned copper profile, in *MATEC Web Conf.*, 2018, p. 01006.
18. A. Laouer *et al.*, *Int. Commun. Heat Mass Transf.* **137**, 106223 (2022).
19. A. Laouer and K. Al-Farhany, *Heat Transf.* **51**, 5952 (2022).
20. F. Aghbalou, F. Badia and J. Illa, *Int. J. Heat Mass Transf.* **49**, 1255 (2006).
21. E.-B. S. Mettawee and G. M. Assassa, *Sol. Energy* **81**, 839 (2007).
22. R. Seeniraj, R. Velraj and N. Lakshmi Narasimhan, *J. Sol. Energy Eng.* **124**, 243 (2002).
23. Y. Zhong *et al.*, *Carbon* **48**, 300 (2010).
24. S. Jegadheeswaran and S. Pohekar, *Int. J. Energy Environ.* **1**, 445 (2010).
25. K. N. Gopal *et al.*, *Int. J. Thermodyn.* **13**, 15 (2010).
26. M. Ghalambaz, K. A. Ayoubloo and A. Hajjar, *Int. J. Numer. Methods Heat Fluid Flow* **30**, 3765 (2019).
27. M. Ghalambaz and J. Zhang, *Int. J. Heat Mass Transf.* **146**, 118832 (2020).
28. G. R. Kefayati, *Int. Commun. Heat Mass Transf.* **40**, 67 (2013).
29. G. Kefayati, *Sci. Iran.* **20**, 1517 (2013).
30. G. Kefayati, *J. Mol. Liq.* **191**, 1 (2014).
31. M. Ghalambaz, M. A. Sheremet and I. Pop, *PLoS One* **10**, e0126486 (2015).
32. M. Sabour and M. Ghalambaz, *Can. J. Phys.* **94**, 604 (2016).
33. G. R. Kefayati, *Int. J. Heat Mass Transf.* **92**, 1066 (2016).
34. G. Kefayati, *Powder Technol.* **299**, 127 (2016).
35. H. Zargartalebi *et al.*, *Numer. Heat Transf. A, Appl.* **70**, 432 (2016).
36. G. Kefayati, *Int. J. Heat Mass Transf.* **108**, 1481 (2017).
37. S. A. Mehryan *et al.*, *Adv. Powder Technol.* **28**, 2295 (2017).
38. M. Ghalambaz *et al.*, *J. Taiwan Inst. Chem. Eng.* **72**, 104 (2017).
39. A. Tahmasebi, M. Mahdavi and M. Ghalambaz, *Numer. Heat Transf. A, Appl.* **73**, 254 (2018).
40. S. Mehryan, M. Ghalambaz and M. Izadi, *J. Therm. Anal. Calorim.* **135**, 1047 (2019).
41. K. K. Al-Chlaihawi *et al.*, *Heat Transf.* **51**, 1725 (2022).
42. K. Al-Farhany *et al.*, *Prog. Nucl. Energy* **145**, 104136 (2022).
43. F. Redouane *et al.*, *Sci. Rep.* **11**, 24316 (2021).
44. M. Ghalambaz, A. J. Chamkha and D. Wen, *Int. J. Heat Mass Transf.* **138**, 738 (2019).
45. M. Ghalambaz, T. Groşan and I. Pop, *J. Mol. Liq.* **293**, 111432 (2019).
46. A. Hajjar, S. Mehryan and M. Ghalambaz, *Int. J. Mech. Sci.* **166**, 105243 (2020).
47. G. R. Kefayati, *J. Mol. Liq.* **195**, 165 (2014).
48. A. Abderrahmane *et al.*, *J. Magn. Magn. Mater.* **562**, 169834 (2022).
49. W. Jamshed *et al.*, *Int. Commun. Heat Mass Transf.* **134**, 106038 (2022).
50. M. Sepyani, A. Shateri and M. Bayareh, *J. Therm. Anal. Calorim.* **135**, 609 (2019).
51. M. Shirazi, A. Shateri and M. Bayareh, *J. Therm. Anal. Calorim.* **133**, 1061 (2018).
52. J. N. Reddy, *An Introduction to the Finite Element Method* (McGraw-Hill, New York, 1993).
53. O. Schenk and K. Gärtner, *Future Gener. Comput. Syst.* **20**, 475 (2004).
54. J. C. De Los Reyes and S. González Andrade, *Numer. Methods Partial Differ. Equ.* **28**, 834 (2012).
55. O. Zienkiewicz, R. Taylor and P. Nithiarasu, *The Finite Element Method for Fluid Dynamics*, 7th edn. (Butterworth-Heinemann, Oxford, 2014).
56. N. H. Abu-Hamdeh *et al.*, *Case Stud. Therm. Eng.* **28**, 101413 (2021).

57. A. A. Ahmadi *et al.*, *Nanomaterials* **10**, 901 (2020).
58. K. Akkoli *et al.*, *Alex. Eng. J.* **60**, 3133 (2021).
59. M. A. Alazwari and M. R. Safaei, *Mathematics* **9**, 881 (2021).
60. M. S. Ali *et al.*, *Case Stud. Therm. Eng.* **23**, 100824 (2021).
61. M. Goodarzi *et al.*, *Alex. Eng. J.* **59**, 4511 (2020).
62. M. Goodarzi *et al.*, *Powder Technol.* **377**, 10 (2021).
63. P. Harari *et al.*, *Case Stud. Therm. Eng.* **25**, 100921 (2021).
64. R. Z. Homod *et al.*, *J. Energy Storage* **34**, 101975 (2021).
65. Z. Li *et al.*, *Int. J. Heat Mass Transf.* **149**, 119124 (2020).
66. Z. Li *et al.*, *Int. J. Heat Mass Transf.* **155**, 119743 (2020).
67. Z. Li *et al.*, *Energy Convers. Manage.* **222**, 113230 (2020).
68. S. Maddah, M. Goodarzi and M. R. Safaei, *Alex. Eng. J.* **59**, 4037 (2020).
69. M. R. Safaei *et al.*, *Case Stud. Therm. Eng.* **28**, 101637 (2021).
70. M. E. M. Soudagar *et al.*, *Appl. Sci.* **11**, 7071 (2021).